Concentration Enrichment in a Dissolving Microdroplet: Accessing Sub-nanomolar Electroanalysis

Ashutosh Rana[a], James Hoang Nguyen[a], Christophe Renault[b] and Jeffrey E. Dick[a,c*]

[a]Department of Chemistry, Purdue University, West Lafayette, IN, 47907, USA
[b]Department of Chemistry and Biochemistry, Loyola University, Chicago, Illinois, 60660, USA
[c]Elmore Family School of Electrical and Computer Engineering, Purdue University, West Lafayette, IN, 47907, USA

*Corresponding Author(s)
Jeffrey E. Dick (jdick@purdue.edu)

Abstract

Droplet evaporation has previously been used as a concentration enrichment strategy; however, the measurement technique of choice requires quantification at rather large volumes. Electrochemistry has recently emerged as a method to robustly probe volumes even down to the attoliter (10^{-18} L) level. We present a concentration enrichment strategy based on the dissolution of a microdroplet placed on the surface of Au ultramicroelectrode (radius ~ 6.25 μm). By precisely positioning a 1,2-dichloroethane microdroplet onto the ultramicroelectrode with a micro-injector, we are able to track the droplet's behavior optically and electrochemically. Because the droplet spontaneously dissolves over time given the relative solubility of 1,2-dichloroethane in the water continuous phase, the change in volume with time enriches the concentration of the redox probe ($Cp_2^*(Fe)^{II}$) in the droplet. We demonstrate the robust electrochemical detection down to sub-nM (800 pM) concentrations of $Cp_2^*(Fe)^{II}$. We note that for this droplet, 800 pM constitutes only about 10^6 molecules. We extend the strategy in a single-blind study to determine unknown concentrations, emphasizing the promise of the new methodology. These results take voltammetric quantification easily to the sub-μM regime.

Introduction

Quantifying trace contaminants is of utmost importance in numerous scientific disciplines, spanning analytical chemistry, environmental science, biomedicine, chemical engineering, and disease diagnostics.[1,2] Even minute concentrations of toxic metals or contaminants can pose significant threats to human health. Moreover, trace elements can exert a profound influence on the properties of engineered devices. Therefore, the development and application of precise measurement techniques for detecting trace analytes is crucial.[3] Presently, a diverse array of analytical techniques exists for ultra-sensitive detection (down to the fM level) of trace analytes. These encompass a variety of approaches, including

spectroscopy-based methods, such as atomic absorption spectrometry (ppb to ppm range), inductively coupled plasma atomic emission spectrometry (ppb to ppm range), and inductively coupled plasma mass spectrometry (ppt to ppb range).[4–6] Additionally, electrochemical techniques, such as potentiometry employing ion-sensitive electrodes and stripping voltammetry (nM to pM range), are widely employed.[7] Furthermore, X-ray-based methods like X-ray fluorescence (ppm to ppb range) are also valuable tools in this regard.[8]

Droplet-based biosensors are gaining attention for their versatility in applications like disease diagnosis and food safety.[9–11] They rely on the evaporation process of sessile droplets to concentrate analytes, especially evident on superhydrophobic substrates where a distinctive coffee-ring pattern forms.[12] This pattern can be harnessed to segregate and concentrate components in biological fluids, aiding diagnostics.[12,13] Surface-enhanced Raman scattering (SERS) is employed for high-sensitivity, label-free detection of trace analytes.[14,15] SERS substrates with closely spaced ultra-sensitive SERS sites have been developed, enhancing detection capabilities.[16–18] This fusion of droplet-based biosensors and SERS technology holds promise across various fields.[19] Evaporation has been used successfully to concentrate an analyte in a droplet for detection using electrochemical methodologies.[20,21] However, any electrochemical measurement requires at least two electrodes that must stay inside the droplet while it is shrinking. This problem has been partially addressed with expensive patterning of the electrodes to control wettability.[12] However, this problem still limits the minimum size of the droplet (and thus pre-concentration and limit of detection) to the size of the two electrodes plus the space between them (several tens of μm).

In this work, we report on the dissolution-driven spontaneous enrichment of redox-active analytes confined in oil droplets submerged in a bulk aqueous phase. We demonstrate electrochemical measurements using cyclic voltammetry in a sub nano-liter (nL) volume of 1,2-dichloroethane (DCE) oil droplets spiked with varying concentrations of decamethyl ferrocene ($(Cp^*)_2Fe^{II}$) dissolving in an aqueous bulk phase of water. To illustrate the concept of concentration enrichment, the dissolution of DCE droplets containing 100 μM of $(Cp^*)_2Fe^{II}$ in an aqueous bulk phase containing 10 mM of $NaClO_4$ was probed using cyclic voltammetry. Our observations revealed intricate changes in the nature of the voltammograms as the droplets dissolved. Specifically, we noted a transition from an initial sigmoidal shape to a duck-shaped curve and finally to a Gaussian pair of peaks (thin-layer behaviour). Concurrently, we observed a significant increase in the magnitude of the observed current throughout the dissolution of the droplet. This transition in the voltammogram's nature provides compelling evidence for the enrichment of analyte concentration as the droplet shrinks to minuscule volumes. We extended this methodology to detect ultra-low concentrations in the nanomolar (nM) regime of $Cp^2{}^*(Fe)^{II}$. Notably, when the droplet is large, voltammograms exhibit no discernible redox activity. However, as the droplet dissolved to negligible volume, we observed a marked increase in current, along with the appearance of redox peaks corresponding to $(Cp^*)_2Fe^{II}$ / $(Cp^*)_2Fe^{III}$. Furthermore, we demonstrated the versatility of this methodology in determining the unknown concentration (sub μM) of $(Cp^*)_2Fe^{II}$ in DCE. Overall, this approach circumvents the limitations associated with droplet evaporation by effectively concentrating the analyte

within the droplet and facilitating its detection using electrochemical methodologies. Droplet evaporation typically necessitates the presence of two electrodes within the droplet. However, in our approach, only a single electrode is required to be present inside the droplet. This simplification not only streamlines the device's design but also facilitates its fabrication process. The key aspect to consider here is that the enrichment of the analyte hinges upon alterations in the droplet's volume. Consequently, any reduction in the dimensions of the electrode, and consequently, the minimum size of the droplet, yields a substantial cubic increase in the enrichment factor. This improvement is directly proportional to the enhancement in the limit of detection. Overall, this work constitutes a significant stride forward in the realm of electrochemical analysis. Its ramifications extend broadly across analytical chemistry and sensor development, promising profound implications for future advancements in these fields.

Experimental Section

All aqueous solutions were prepared using ultra-pure deionized water with a resistivity of 18.2 MΩ.cm, sourced from a GenPure water purification system manufactured by Millipore. The organic solvent 1,2-dichloroethane, 99.8% purity (DCE) was acquired from Sigma Aldrich. The salts for all the experiments; decamethyl ferrocene (Cp^*), was obtained from Sigma Aldrich. Potassium chloride (KCl) was obtained from Fisher Bioreagents. All reagents were of analytical grade and were used without any additional purification. Prior to experimentation, the glassware underwent meticulous cleaning using mQ water, followed by acetone (99.9%, Sigma-Aldrich), and finally with the relevant solvent for each solution. Gold working electrodes with a diameter of 12.5 μm were obtained from CH Instruments, while the Ag/AgCl reference electrode (CH Instruments) in 1 M KCl was employed as the counter/reference electrode. Before usage, the working electrodes were polished with a 0.3 μm alumina powder suspension (Electron Microscopy Sciences) on micro-cloth polishing pad (Buehler) using water. Subsequently, they underwent a cleaning process with piranha solution, which was a mixture of concentrated sulfuric acid with 30% hydrogen peroxide in a 2:1 ratio, to ensure thorough purification. The lab-made electrochemical cell, constructed out of Teflon, was also carefully cleaned using Piranha solution to eliminate any potential impurities. Microinjection experiments were performed using a micro-injector (FemtoJet 4i Eppendorf) and microinjection capillary tips with an orifice diameter of 10 μm (Eppendorf Femtotips). The position of the microinjector was controlled using an XYZ micro-positioning system (InjectMan 4) and monitored with an optical microscope equipped with a high-resolution sCMOS camera (C15440 Orca Fusion BT). All electrochemical experiments were conducted using a CHI 6284E potentiostat (CH Instruments). The reference electrode was placed in a separate compartment containing 1 M KCl and was connected to the cell through a salt bridge.

The salt bridge was created by filling a glass tube with 3% agarose (99.9%, Sigma-Aldrich) containing 1 M potassium chloride.

Results and Discussion

This section delves into the intricacies of performing electrochemical measurements within a sub nL volume DCE droplet dissolving in an aqueous bulk phase. It is divided into three interconnected sections. Firstly, we explore the methodology employed for the enrichment of concentration resulting from the dissolution of the oil droplet, utilizing voltammetry as a probing technique. Secondly, we investigate the detection of redox analytes at ultra-low concentrations, typically within the nM range. This section highlights the remarkable capability of our technique to detect and quantify such minute concentrations, which is beyond the reach of conventional bulk voltammetric measurement methods. Finally, we demonstrate the precision of our method in quantifying unknown concentrations of redox analytes, even when they exist at sub-micromolar (sub- μM) levels.

- **Methodology of Enrichment in Concentration in a Dissolving Reactor**

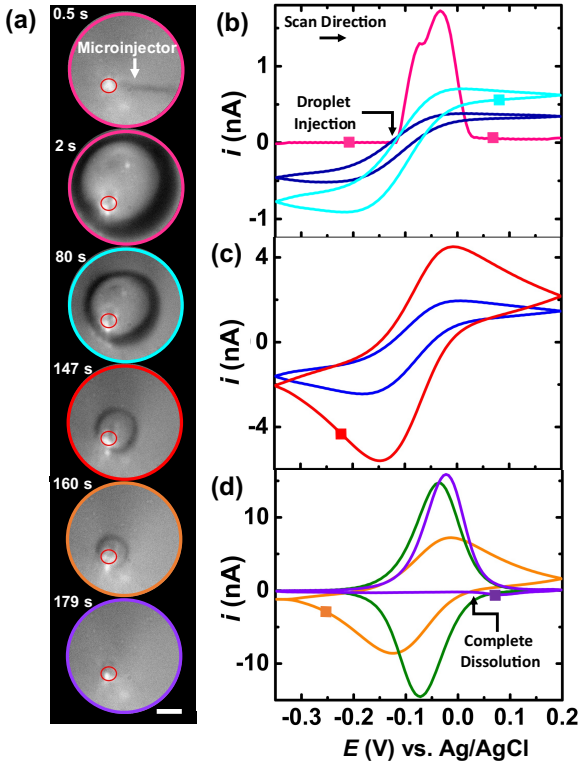

Figure. 1 (a) Optical micrographs recorded during the dissolution of a 41 ± 3 μm radius droplet containing 100 μM of $(Cp^*)_2Fe^{(II)}$ in a 10 mM $NaClO_4$ aqueous bulk phase. The scale bar is 25 μm. Pannels (b), (c) and (d) show cyclic voltammograms recorded simulatenously with the optical micrographs during the dissolution of the 100 μM $Cp^*_2(Fe)^{II}$ containing DCE droplet. The scan rate is $\nu = 0.2$ V/s. The color code used for the cyclic voltamogramms matches the color code in (a), denoting the the size of the droplet during that segment of the CV. The square marked points (■) points on the cyclic voltammogram indicate

the exact time when the frames in (a) were recorded. A total of 33 voltammograms were recorded during the entire experiment. Panel **(b)** shows CV 1, 7 and 15, Panel **(c)** shows CV 23 and 27, Panel **(d)** shows 29, 32 and 33.

The effect of the dissolution of the droplet containing 100 μM $(Cp^*)_2Fe^{II}$ in DCE in an aqueous bulk phase containing 10 mM of $NaClO_4$ was probed using voltammetry, as shown in **Fig. 1**. The detailed experimental methedology can be found in our previously reported works.[22,23] Wherein, a microinjector system equipped with a xyz micropositioner and micropipette loaded with a redox active analyte, $Cp_2^*(Fe)^{II}$ in DCE was used to deposit tiny microdroplets on the 12.5 μm diameter Au UME. The setup was equipped with high-resolution optical camera which enabled precise positioning of the microcapillary and observing the effect of dissolution on the size of the droplet with time. All of the electrochemical measurements were performed on a two electrode setup where Au UME served as the working electrode and Ag/AgCl in 1M KCl served as the refernce/counter electrode.

The potential of the UME was constantly scanned between an initial potential of -0.35 V to 0.2 V at a scan rate of 0.2 V/s (see the arrow of the scan direction in panel **(b)** of **Fig. 1**). **Fig. 1(a)** shows the series of optical micrographs recorded during a typical experiment. The solid red circle at the center of the micrographs denote the position of the Au disk. The time has been referenced from $t = 0$ s, indicating the start of the experiment i.e., time synchronised optical microscopy and voltammetry. Before the injection of the droplet, the microinjector is aligned in close proximity of the electrode, evident from micrograph recorded at 0.5 s which shows the exact position of the microinjector. The initial size of the droplet was measured to be 41 ± 3 μm from micrograph recorded at 2 s. The series of micrographs shown in **Fig. 1(a)** show that the DCE droplet spontaneously dissolves with time in the bulk aqueous phase within 177 ± 2 s. This time is measured based on the time difference between time corresponding to initial droplet injection (t =2 s) and time at which the droplet appears to shrinks to a zero volume (t =179 s). The exact time of zero volume is difficult to track as the droplet shrinks to dimensions below the sub-diffraction limit. The effect of the dissolution of the droplet on the nature of voltammograms is evident from panel **(b)**, **(c)**, and **(d)** in **Fig. 1**. The potential windows were chosen such that the apparent standard potential of the redox couple $(Cp^*)_2Fe^{(III)}/(Cp^*)_2Fe^{(III)}$ (E'= –0.10 V) was centered around the potential window of voltammetry.[23] The colored points and current traces in panel **(b)**, **(c)**, and **(d)** in **Fig. 1** correspond to the time when the micrographs in **Fig. 1 (a)** were recorded. The pink voltammograms on panel (a) in **Fig. 1** marks the initial baseline in the absence of a droplet. The affect of droplet injection is marked with an abrupt increase in current due to oxidation of $(Cp^*)_2Fe^{(II)}$ to $(Cp^*)_2Fe^{(III)}$. The injection of droplet appears as positive surge of current as during injection induces a massive flux of $(Cp^*)_2Fe^{(II)}$ at the electrode surface. It's important to note that the injection of the droplet is not an extremely fast process compared to the voltammetric scan. This difference results in convection, leading to a sudden massive flux of $(Cp^*)_2Fe^{(II)}$ at the electrode surface, which results in the oxidation of $(Cp^*)_2Fe^{(II)}$ to $(Cp^*)_2Fe^{(III)}$ as the potential is sufficiently positive to facilitate the oxidation of $(Cp^*)_2Fe^{(II)}$ to $(Cp^*)_2Fe^{III}$. The complete dissolution of the droplet appears as a sudden decrease in current as shown by the purple voltammogram in panel **(d)** of **Fig. (a)**. After the complete dissolution of the droplet, current returns to the initial baseline current

recorded prior to the droplet injection. The characteristics and the intensity of the voltammogram changes as a function of droplet size. We initially observe a sigmoid shaped voltammogram (blue and cyan curve on **Fig. 1 (b)**) when the droplet size is large. This behaviour is typical of an UME due to the large droplet size mimicking bulk like condition.[24] The steady state current for anodic and cathodic sweeps on the blue voltammogram in panel **(a)** was observed to be 0.3/ 0.5 nA, respectively. It was shown in our previous work that when the droplet is large (bulk-like condition), the redox activity is confined in a very close proximity of the electrode surface and does not reach the boundary of the dissolving reactor.[23] However, as the droplet gets smaller in volume we notice the appearence of peaks on the voltammograms (navy and red curves on panel **(c)** of **Fig. 1**). This "peaking" behaviour gets more pronounced with time, eventually leading to Gaussian-shaped pair of peaks reaching a current of almost $\pm$ 10 nA (olive green voltammogram on panel **(d)** of **Fig. 1**). These gaussian shaped peaks imply that the droplet reaches a thin-layer like condition where the size of the droplet is compare to the size of the electrode and voltammetry can probe all of the redox active molecules present in the reactor.[23] It is crucial to realise that the magnitide of observed current in the system during voltammetric scans is sensitive to the volume of droplet. As observed, the overally current in system increases with the dissolution of the droplet, providing a strong evidence for spontaneous enrichment of the redox probe confined in the dissolving reactor. Nonetheless, these intricate changes in the nature of voltammogram will only be observed if the analyte does not partition across the DCE|water interface and leave the droplet This also explain the choice of the redox analyte, ($Cp_2^*(Fe)^{II}$) in this work as it does not dissolve in water and is expected to partition strongly in the DCE droplet.

In **Fig. 2**, we provide a schematic illustration depicting the enrichment methodology for the dissolving droplet shown in **Fig. 1**. In general, the enrichment in analyte concentration relies on the total number of redox active molecules confined in the droplet, which in turn depends on two factors: the initial volume of the droplet dispensed onto the Au disk and the initial concentration of the analyte within the droplet. Throughout the entire dissolution process, the number of molecules or moles of the redox analyte confined within the droplet remains conserved, assuming no partitioning of the analyte across the oil/water interface. Consequently, this conservation leads to a substantial enrichment in the analyte concentration within the reactor. As shown in **Fig. 2**, the initial concentration, 100 μM, and volume, 0.28 nL, of the droplet shown in **Fig. 1** correspond to 28 picomoles of redox-active molecules confined within it. Our previous work has demonstrated that as the droplet approaches its complete dissolution, it accesses volumes in the picoliter (pL) range.[23] This results in a final concentration in the range of tens of millimolars (28 mM), yielding an enrichment factor exceeding two orders of magnitude. In the subsequent sections, we employ this enrichment strategy to significantly enhance the sensitivity of voltammetry. This enhancement allows us to probe ultra-low concentrations (nM range) of the analyte, a feat unattainable through conventional bulk voltammetric measurements.

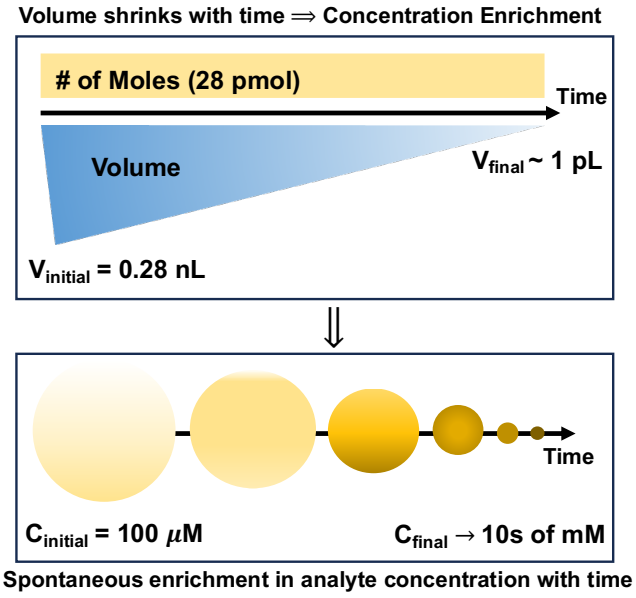

Figure. 2 Schematic illustrating the process of spontaneous pre-concentration of analyte in a dissolving reactor

- **Detection of Ultra-low Concentration (nM) of Redox Analyte**

We demonstrate detection of ultra-low concentration of 10 nM $Cp_2^*(Fe)^{II}$ in DCE based on the enrichment strategy detailed above. **Fig. 3 (a)**, shows the dissolution of a DCE droplet containing 10 nM $Cp_2^*(Fe)^{II}$. Similar to the previous case, the time has been refernced from t = 0 s. The initial droplet size was measured to be 64 ± 3 μm based on the micrograph recorded at t = 0.5 s. During the entire course of dissolution the droplet remains centered around the Au disk as the three-phase boundary gets pinned at the Au/glass interface forcing the droplet to stay centered on the UME. Voltammetry was performed between the same potential windows and scan rate as **Fig. 1**. Voltammograms recorded during the dissolution of the droplet is shown **Fig. 3 (b)** and **(c)**. In the presence of the large oil droplet, no redox activity for $(Cp^*)_2Fe^{(II)}/(Cp^*)_2Fe^{(III)}$ is observed around the $E^{o'}$ (-0.1 V vs. Ag/AgCl), as shown by the pink, blue and green curves on **Fig. 3 (b) and (c)**. However, we record an notable increase in the current surge as the droplet further dissolves (orange voltammogram in **Fig. 3 (c)**). This is due to enrichment of the redox analyte in the droplet. As the droplet accesses tinier volumes, the the magnitide of current further increases and redox peaks can be observed at the apparent standard potential of the redox couple (purple voltammogram on **Fig. 3 (c)**). The transition from no redox activity to the presence of characteristic signals around $E^{o'}$ is gradual and occurs over several voltammetric cycles. As observed in the previous case of 100 μM $Cp_2^*(Fe)^{II}$, the magnitude of current increases as the droplet shrinks to negligible volumes. Therefore, right before the complete dissolution of the droplet we see bell-shaped voltammogram (purple curve on **Fig. 3 (c)**), indicating thin-layer like condition, where all of the redox active molecules in the reactor can be probed. The green highlighted region on **Fig. 3 (c)** denotes the position on the voltammogram concerning the appearance of redox activity of $(Cp^*)_2Fe^{(II)}/(Cp^*)_2Fe^{(III)}$. The

color bar depicted in **Fig. 3 (a)** is included solely for qualitative purposes, serving to illustrate the concept of analyte enrichment and the emergence of redox activity for $(Cp^*)_2Fe^{II}/(Cp^*)_2Fe^{III}$. During the course of the experiment, a total of 78 voltammograms were recorded. **Fig 3 (b)** shows CV 1 and 15, and **Fig. 3 (c)** shows CV 34, 67 and 71. CV 71 shows the highest redox activity (in terms of the magnitude of peak current). The voltammograms (CV 72–78) recorded between 387 s and 408 sec (last two micrographs in panel **(a)** of **Fig. 3**) is shown in **Fig. S1**, wherein the peak currents reduce as we progess in time, eventually leading to the complete dissolution of the droplet. In this work, we abstain from quantifying the charge for all the voltammograms since there is no abrupt transition from no redox activity to the appearance of detectable peaks at the apparent standard potential of the redox couple $(Cp^*)_2Fe^{(II)}/(Cp^*)_2Fe^{(III)}$ ($E^{\circ\prime}$ = –0.10 V). Instead, we concentrate on the last voltammogram, specifically the one obtained during the thin-layer regime right before the complete dissolution of the droplet. This particular voltammogram, characterized by the highest peak current and charge, is chosen for charge quantification. The experimentally detected charge based on the purple voltammogram (see the details in **SI Pg. no 3**) is found to be an order of magnitude higher than the expected value. We noticed in several independent experiments (with 10 nM $Cp^*_2(Fe)^{II}$) that the experimentally measured charge was always higher by one to two orders of magnitude than the expected value. Given the reproducibility of the result, our confidence in our ability to measure out known amounts and successfully dilute, and the fact that the wave appears at the expected formal potential of our redox species, this observation does not detract from our main claim of quantifying nM amounts of a redox analyte. The discrepancy likely arises due to the notorious reactivity of $Cp^*_2(Fe)^{II}$ with oxygen at the oil-water interface leading to complex reaction pathways.[25] Elucidating this mechanism will be the topic of a future investigation.

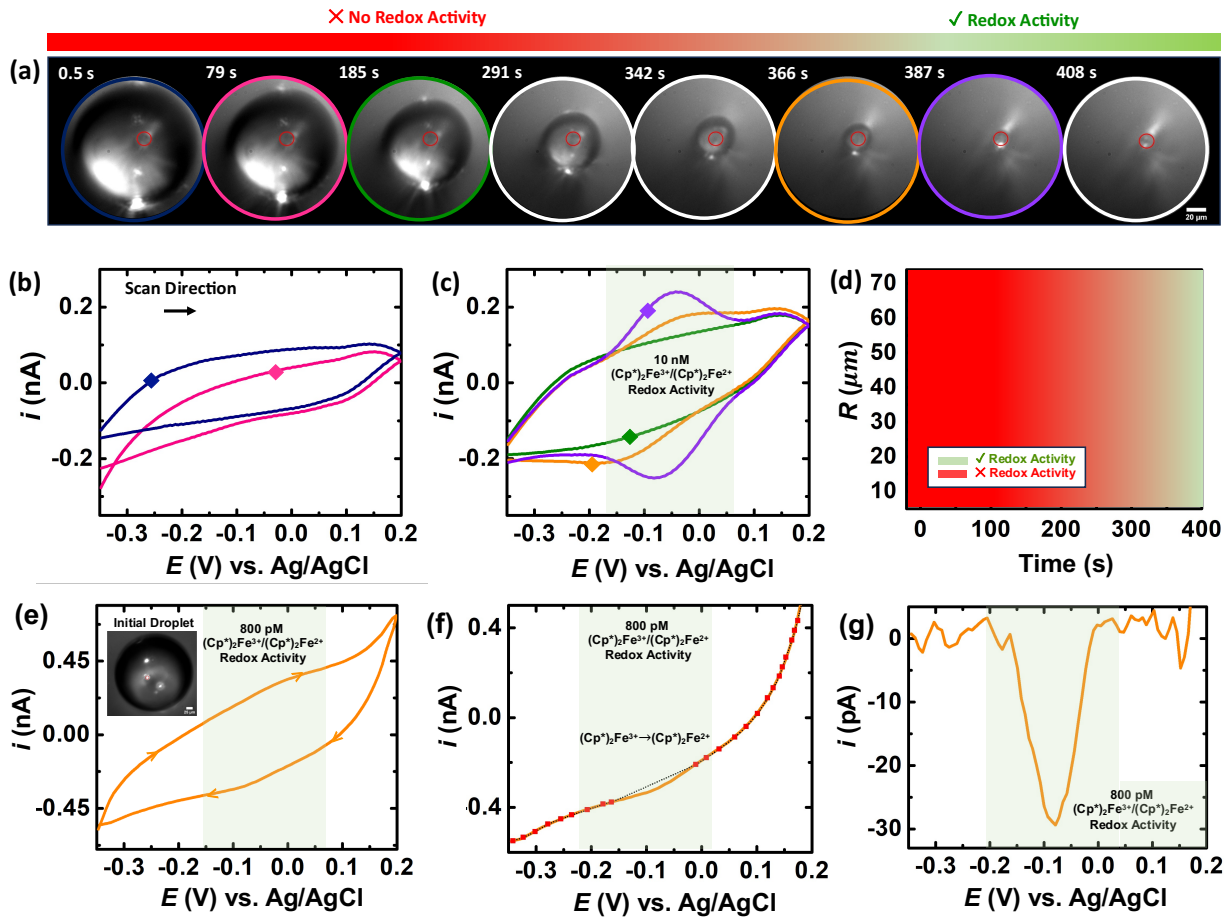

Figure. 3 (a) Optical micrographs recorded during the dissolution of a 60 ± 2 μm radius droplet containing 10 nM of $(Cp^*)_2Fe^{(II)}$ in a 10 mM $NaClO_4$ aqueous bulk phase. Panels (b) and (c) show cyclic voltammograms recorded simultaneously with the optical micrographs during the dissolution of the 10 nM $(Cp^*)_2Fe^{II}$ containing DCE droplet. The scan rate is $\nu = 0.2$ V/s. The color code used for the cyclic voltammograms matches the color code in (a), denoting the size of the droplet during that segment of the CV. The square marked points (■) points on the cyclic voltammogram indicate the exact time when the frames in (a) were recorded. (d) Apparent droplet's radius as a function of time measured from the optical micrographs in (a), marking the appearance of redox activity of $(Cp^*)_2Fe^{(II)}$/ $(Cp^*)_2Fe^{(III)}$. (e) Cyclic voltammogram captured during the dissolution of a droplet of DCE containing 800 pM of the $(Cp^*)_2Fe^{(II)}$/ $(Cp^*)_2Fe^{(III)}$ at a scan rate of 1 V/s, indicating the presence of redox activity. The initial droplet size is illustrated in the inset (measured as 154 ± 2 μm). (f) The baseline for the voltammogram is manually constructed, as depicted by the dashed black line, and is utilized for integrating the charge under the reverse sweep of the voltammogram presented in (e). (g) The voltammogram is baseline-corrected, directly derived from the baseline correction performed in (f).

Fig. 3 (d) shows the evolution of apparent radius of the droplet as a function of time which details the occurrence of redox activity with the decreasing size of the droplet. Note that detection of 10 nM $Cp_2^*(Fe)^{II}$ in DCE is not possible using the conventionally used bulk cyclic voltammetry measurements using a microelectrode. **Fig. S2** shows the voltammogram recorded in a bulk solution of 10 nM $Cp_2^*(Fe)^{II}$ in DCE in a similar two-electrode configuration, showing the absence of any form of redox activity. Therefore, using the technique detailed in this work i.e., enrichment of a analyte in a dissolving reactor, we can achieve nM level of quantification in cyclic voltammetry. Nonetheless, it is crucial to realise that a larger initial volume (which

scales proportionally to the number of molecules of anaylte confined in the reactor) of the droplet will give us a higher enrichment facor. For instance, the time after which we can clearly see signals arising from the redox activity of 10 nM $Cp_2^*(Fe)^{II}$ in DCE in **Fig. 3 (d)** could be pushed to an earlier time if the initial volume of the droplet were larger. From various studies in the field of evaporation/ dissolution of sessile droplets it is known the rate of dissolution accelerates as the droplet gets smaller in size.[26,27] Alongside the accelerated dissolution rate, the maximum enrichment is concentration (a higher probability of detection) of the analyte is also achieved when the droplet accesses negligible volumes. One might wonder about the minimum concentration of the redox analyte that can be detected using this methodology on the same experimental setup. In **Fig. 3 (e)**, the cyclic voltammogram recorded during the dissolution of a DCE droplet containing 800 pM of $(Cp^*)_2Fe^{(II)}$/ $(Cp^*)_2Fe^{(III)}$ is shown. We note that for this droplet, 800 pM constitutes only about 10^6 molecules. The initial droplet geometry is depicted as an inset image in **Fig. 3 (a)**, where the initial radius was measured to be 154 ± 2 μm. The initial charge confined in the droplet was calculated to be approximately 1.2 pC. Notably, a scan rate of 1 V/s was employed, in contrast to the earlier 0.2 V/s. The deliberate choice of a higher scan rate aims to increase the likelihood of capturing signals from the redox molecules, thereby maximizing the chances of detecting the signal as the droplet undergoes rapid dissolution as it gets smaller. However, this choice comes with the trade-off of an increased capacitive current resulting from the charging/discharging of the double-layer. Similar to the case of 10 nM, no redox activity was detected until the droplet dissolved to tiny volumes. The voltammogram shown in **Fig. 3 (e)** illustrates the cycle where redox activity becomes observable for the 800 pM case. For the analysis of the detected charge, the reverse sweep was of the voltammogram shown in **Fig. 3 (e)** was selected, and a baseline was constructed as indicated by the black-dotted curve in **Fig. 3 (f)**. Following baseline correction, a clear indication of the presence of redox activity emerges at the apparent standard potential for the redox couple, with a detected charge of approximately 2.3 pC. It is noteworthy that, akin to the previous case of 10 nM, the observed charge value is higher than the expected value. **Fig. S3** shows a similar outcome for the detection of 1 nM of the redox analyte, where voltammetry was recorded in a comparable manner at a scan rate of 1 V/s for a dissolving DCE droplet containing 1 nM analyte with an initial radius of 65 ± 2 μm (initial charge: 0.12 pC). The orange curve illustrates the voltammetry when the droplet was large, while the solid navy curve depicts the voltammogram wherein the maximum redox activity was detected. Through charge integration, a detected charge of 4.5 pC was observed. For the 800 pM case, the 1.2 pC of charge was detected using voltammetry. This value is still lower than the detected charge (4.5 pC) for the 1 nM result shown in **Fig. S3**, despite the smaller size of the droplet and similar initial concentrations. This may be due to the uncontrolled dynamics of dissolution of the droplet or partitioning of $(Cp^*)_2Fe^{II/III}$ molecules into the water phase during the dissolution process. This phenomenon is anticipated to be more pronounced in the larger droplet, as its increased size significantly extends the droplets' lifetime, allowing for enhanced partitioning of the $(Cp^*)_2Fe^{II/III}$ molecule into the water phase. This assertion is further substantiated by the data discussed later in **Table**

1, where a larger droplet exhibits a lower detected charge compared to the initial charge for the same concentration of $(Cp^*)_2Fe^{II}$ initially confined within the droplet.

Achieving higher sensitivity, beyond sub-nanomolar levels, through voltammetry necessitates a high temporal resolution to probe redox activity during the final moments of the droplet. This constitutes one route of tuning analytical figures of merit of this proposed method. However, in the current experimental setup, the capacitive current scales up with increased temporal resolution, resulting in a substantial background current that complicates ultra-sensitive measurements. In principle, the idea of increased temporal resolution with lower capacitive currents may be achieved by employing fast scan cyclic voltammetric measurements using nanoelectrodes, representing a future avenue of our research.

- **Determining Unknown Concentration of Redox Analyte (sub μM levels)**

In bulk voltammetric measurement using an UME, it is difficult to determine concetration of a redox analytes based on the steady state current response for analyte concentrations below the μM levels, as we run into a fundamental problem of a lower signal to noise ratio. For instance, the steady-steady current response to a disk UME is given by $i_{ss} = 4nFDCr$ where, n is the number of electrons, F is the Faradays constant, D is the diffusion coefficicnet of the redox species in the solvent and r is the radius of the UME.[24] Considering $Cp_2^*(Fe)^{II}$/ $Cp_2^*(Fe)^{III}$ as the redox couple, $n = 1, F = 96500\ C/mol, D = 0.8 \text{ x} 10^{-5}\ cm^2/s$, $C = 1\ \mu M$ and $r = 6.26\ um$, yielding $i_{ss} \sim 20\ fA$. The typical noise level while using a UME are on the order of 10s of fA at best. We therefore do not expect to observe such a concentration in bulk. In this section, we show how the methodology detailed in this work can allow us to quantify unknown anaylte concentrations in the sub μM regime, using a test solution of 800 nM $Cp_2^*(Fe)^{II}$ in DCE. We performed a single-blind study, where one lab member made a known concentration of $Cp_2^*(Fe)^{II}$ in DCE, and another lab member confirmed the concentration with the dissolving microdroplet method. We refer to this solution as the unknown test sample. Similar experiments were performed as detailed in the preceding sections using the unknown test sample. The electrochemical response for the dissolution of a 48 ± 3 μm droplet (**Fig. 4 (a)**) is shown in **Fig. 4 (b)**. The voltammograms corresondong to the micrographs recorded at 2 s and 7 s are shown in the **Fig. S3 (a)** (CV1 and CV2, respectively), showing no detectable redox activity for $Cp_2^*(Fe)^{II/III}$. As expected, we see no detectable redox activity until droplet accesses extremely tiny volume (purple curve in **Fig. 4 (b**)). A total of 47 voltammograms were recorded during the entire experiments (orange curve: CV 27, and purple cuve: CV 39). CVs beyond CV 39 are shown in **Fig. S3 (b)**, where the redox activity shuts off with time. **Movie S1** shows the side-by-side depiction of the droplet size along with the concurrent evolution of the voltammogram for the data presented in **Fig. 4**, illustrating the emergence of redox activity as the droplet gradually shrinks over time. Based on voltammrams it was identified that the maximum redox activity (thin-layer regime) was probed in CV 39 (purple curve). Faraday's law was used to deduce the initial concentration of the redox analyte based on the value of charge

and the initial volume of the droplet. The details of the calculation can be found on **SI Pg. no 5**. The initial volume was calculated to be 0.45 nL. **Fig. 4 (c)** shows the amount of charge probed based on the current response, and was measured to be 24 pC. Using these values, the concentration of the analyte in the unknown test sample was ~500 nM (which equates to a relative error of ~35 %). This error likely originates from the partitioning of $Cp_2^*(Fe)^{II/III}$ species across the oil/water interface into the aqueous bulk phase. The relative error can be minimized by speeding up the dissolution process or accounting for the partitioning kinetics at the oil|water interface. Given the low concentrations, the measurement precision is quite robust even with this effect.

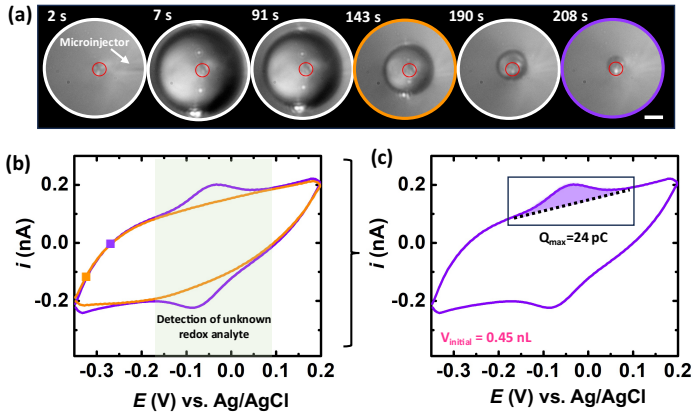

Figure. 4 (a) Optical micrographs recorded during the dissolution of a 48 ± 3 μm radius DCE droplet containing 800 nM of $(Cp^*)_2Fe^{(II)}$. The scale bar is 20 μm. (b) Cyclic voltammograms recorded simulatenously with the optical micrographs during the dissolution of the 10 nM $(Cp^*)_2Fe^{II}$ containing DCE droplet; orange: CV 27 and purple: CV 39. (c) Calculation of charge based on CV 39. The initial volume of the droplet was 0.45 nL.

The methodology elucidated in this work establishes a robust foundation for the detection and quantification of sub-micrometer levels of redox analytes. While it might be intuitive to assume that employing a larger initial droplet size would lead to higher analyte enrichment, given the reliance on droplet dissolution in the overall strategy, this assumption is not always straightforward. Larger droplet sizes can indeed enhance enrichment, but they often contend with the partitioning of redox analytes into the bulk phase, particularly in scenarios where the droplet size is significant (resulting in a longer droplet lifetime) and the analytes have ample time to partition across the oil|water interphase into the bulk aqueous phase. A straightforward analysis, comparing the initial charge confined in the droplet to the amount of charge detected during the thin-layer behaviour, allows us to gain insights into this phenomenon.

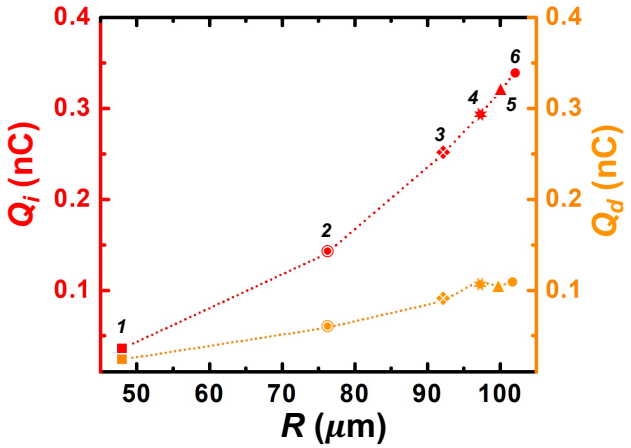

Figure 5. Comparison of Initial Confined Charge (Q_i) within the Droplet and Detected Charge (Q_d) as a Function of Initial Apparent Radius (R). The data comprises points 1-6, each representing independent experiments. Point 1's data is extracted from Fig. 4, while the datasets for points 2-6, used to determine Q_i, Q_d, and R, are presented in Fig. S4.

Fig. 5 presents a comparison between the initial charge (Q_i) confined in the droplet, calculated according to Faraday's law, and the detected charge (Q_d), obtained by integrating the change in the recorded voltammogram during the thin-layer behavior, plotted against the initial apparent radius (R) of the droplet. Each data point on the plot is labeled from 1 to 6, corresponding to independent experimental runs. Notably, when the droplet size is small, the disparity between Q_i and Q_d is minimal. However, as the droplet size increases, these differences become more pronounced. This strongly implies significant partitioning of $Cp_2^*(Fe)^{II}$/ $Cp_2^*(Fe)^{III}$ species into the bulk phase during droplet dissolution. The exact values for the initial radius of the droplet, Q_i, and Q_d are provided in **Table 1**. As anticipated, droplets with a greater initial radius exhibit higher Q_i values, but the proportion of charge detected in voltammetry diminishes with increasing droplet size. Specifically, Point 1 in **Fig. 5** and **Table 1** represent the dataset from **Fig. 4** (R= 48 μm), where ~35% of $Cp_2^*(Fe)^{II}$/ $Cp_2^*(Fe)^{III}$ partitions into the bulk aqueous phase. This value increases to ~66% for a droplet with an initial radius of 102 μm. In summary, this observation underscores that the limit of detection for the system is influenced by two primary factors: the number of redox-active moles confined to the droplet and their relative partitioning kinetics into the bulk phase.

Table 1. Comparison between the initial apparent radius (R) of the droplet, initial charge confined in the droplet (Q_i), detected charge based on the voltammogram (Q_i), and ratio of Q_d to Q_i.

Sl. no	R (um)	Q_i (nC)	Q_D (nC)	Q_D / Q_i (%)
1	48	0.036	0.024	0.66
2	76	0.140	0.059	0.42
3	92	0.249	0.088	0.35

4	97	0.291	0.110	0.38
5	100	0.319	0.104	0.33
6	102	0.339	0.111	0.33

Conclusion

In summary, our study demonstrates the electrochemical analysis of sub nL volume oil droplets as they dissolve in an aqueous phase. We employed cyclic voltammetry to track the changing voltammogram shape during dissolution, revealing a fundamental shift in electrochemical behavior, transition from an initial sigmoid to bell-shaped curves with a significant increase in the magnitude of current. This occurs due to enrichment in analyte's concentration in the droplet thereby, enhancing their concentration by several orders of magnitude within minutes. We demonstrate the detection of sub-nM levels of redox analyte using the methodology, showcasing its potential for trace analyte sensing. This technique holds promise for applications involving the detection of trace biomolecules, heavy metals, and nanoparticles, offering enhanced sensitivity and precision. Moreover, we also demonstrate quantification of analyte concentration in the sub-uM range using cyclic voltammetry. Overall, this work represents a significant advancement in electrochemical analysis with wide-ranging implications in analytical chemistry and sensor development.

Acknowledgments

This work was funded by the Chemical Measurement and Imaging Program of the National Science Foundation under grant CHE-2003587/2319925

Author Contribution

A.R. and J.H.N contributed equally to this work. A.R. conducted all the experiments, while J.H.N. carried out the sub-nanomolar detection experiments. A.R., J.H.N., C.R., and J.E.D. collaborated on writing the manuscript. J.E.D. supervised the overall project.

Supplementary Information

Cyclic voltammograms no. 71, 72, 73 and 78 recorded during the dissolution of DCE droplet containing 10 nM $(Cp^*)_2Fe^{II}$, Experimentally probed charge for 10 nM $(Cp^*)_2Fe^{II}$ containing DCE droplet, Cyclic voltammogram for 10 nM $(Cp^*)_2Fe^{II}$ in DCE in bulk, Cyclic voltammograms recorded during the dissolution of DCE droplet containing 800 nM $(Cp^*)_2Fe^{II}$ (CV 1,2 39, 42

and 47), Experimentally probed charge for 800 nM $(Cp^*)_2Fe^{II}$ containing DCE droplet, Initial droplet size and corresponding voltammograms for points 2-6 in Table 1 and Fig. 5 in main file.

References

(1) Cecchini, M. P.; Turek, V. A.; Paget, J.; Kornyshev, A. A.; Edel, J. B. Self-Assembled Nanoparticle Arrays for Multiphase Trace Analyte Detection. *Nat Mater* **2013**, *12* (2), 165–171. https://doi.org/10.1038/nmat3488.

(2) Crosby, D.; Bhatia, S.; Brindle, K. M.; Coussens, L. M.; Dive, C.; Emberton, M.; Esener, S.; Fitzgerald, R. C.; Gambhir, S. S.; Kuhn, P.; Rebbeck, T. R.; Balasubramanian, S. Early Detection of Cancer. *Science*. American Association for the Advancement of Science March 18, 2022. https://doi.org/10.1126/science.aay9040.

(3) Bulska, E.; Ruszczyńska, A. Analytical Techniques for Trace Element Determination. *Physical Sciences Reviews* **2017**, *2* (5). https://doi.org/10.1515/psr-2017-8002.

(4) Rahman, S.; Waheed, S. Blood-Copper and Zinc Levels and Consequences of Cardiovascular Complications: A Study by INAA and FAAS. *J Radioanal Nucl Chem* **2011**, *287* (2), 657–664. https://doi.org/10.1007/s10967-010-0843-7.

(5) Siddique, N.; Majid, A.; Chaudhry, M. M.; Tufail, M. Determination of Heavy Metals in Air Conditioner Dust Using FAAS and INAA. *J Radioanal Nucl Chem* **2012**, *292* (1), 219–227. https://doi.org/10.1007/s10967-011-1402-6.

(6) Özdemir, C.; Saçmaci, Ş.; Kartal, Ş. A Coprecipitation Procedure for the Determination of Some Metals in Food and Environmental Samples by Flame Atomic Absorption Spectroscopy. *Analytical Methods* **2013**, *5* (16), 3977–3983. https://doi.org/10.1039/c3ay40727f.

(7) Alves, G. M. S.; Magalhães, J. M. C. S.; Salaün, P.; van den Berg, C. M. G.; Soares, H. M. V. M. Simultaneous Electrochemical Determination of Arsenic, Copper, Lead and Mercury in Unpolluted Fresh Waters Using a Vibrating Gold Microwire Electrode. *Anal Chim Acta* **2011**, *703* (1), 1–7. https://doi.org/10.1016/j.aca.2011.07.022.

(8) Strange, R. W.; Feiters, M. C. Biological X-Ray Absorption Spectroscopy (BioXAS): A Valuable Tool for the Study of Trace Elements in the Life Sciences. *Current Opinion in Structural Biology*. October 2008, pp 609–616. https://doi.org/10.1016/j.sbi.2008.06.002.

(9) Yang, G.; Xiao, Z.; Tang, C.; Deng, Y.; Huang, H.; He, Z. Recent Advances in Biosensor for Detection of Lung Cancer Biomarkers. *Biosensors and Bioelectronics*. Elsevier Ltd September 15, 2019. https://doi.org/10.1016/j.bios.2019.111416.

(10) Zhou, Q.; Tang, D. Recent Advances in Photoelectrochemical Biosensors for Analysis of Mycotoxins in Food. *TrAC - Trends in Analytical Chemistry*. Elsevier B.V. March 1, 2020. https://doi.org/10.1016/j.trac.2020.115814.

(11) Park, H.; Li, S.; Niu, G.; Zhang, H.; Song, Z.; Lu, Q.; Zhang, J.; Ma, C.; Kwok, R. T. K.; Lam, J. W. Y.; Wong, K. S.; Yu, X.; Xiong, Q.; Tang, B. Z. Diagnosis of Fatty Liver Disease by a Multiphoton-Active and Lipid-Droplet-Specific AIEgen with Nonaromatic Rotors. *Mater Chem Front* **2021**, *5* (4), 1853–1862. https://doi.org/10.1039/d0qm00877j.

(12) Wang, Y.; Liu, F.; Yang, Y.; Xu, L. P. Droplet Evaporation-Induced Analyte Concentration toward Sensitive Biosensing. *Mater Chem Front* **2021**, *5* (15), 5639–5652. https://doi.org/10.1039/d1qm00500f.

(13) Wong, T. S.; Chen, T. H.; Shen, X.; Ho, C. M. Nanochromatography Driven by the Coffee Ring Effect. *Anal Chem* **2011**, *83* (6), 1871–1873. https://doi.org/10.1021/ac102963x.

(14) Kneipp, K.; Wang, Y.; Kneipp, H.; Perelman, L. T.; Itzkan, I.; Dasari, R. R.; Feld, M. S. *Single Molecule Detection Using Surface-Enhanced Raman Scattering (SERS)*; 1997.

(15) Lindquist, N. C.; de Albuquerque, C. D. L.; Sobral-Filho, R. G.; Paci, I.; Brolo, A. G. High-Speed Imaging of Surface-Enhanced Raman Scattering Fluctuations from Individual Nanoparticles. *Nat Nanotechnol* **2019**, *14* (10), 981–987. https://doi.org/10.1038/s41565-019-0535-6.

(16) Kim, Y. J.; Lee, G. R.; Cho, E. N.; Jung, Y. S. Fabrication and Applications of 3D Nanoarchitectures for Advanced Electrocatalysts and Sensors. *Advanced Materials*. Wiley-VCH Verlag September 1, 2020. https://doi.org/10.1002/adma.201907500.

(17) Ding, Q.; Wang, J.; Chen, X.; Liu, H.; Li, Q.; Wang, Y.; Yang, S. Quantitative and Sensitive SERS Platform with Analyte Enrichment and Filtration Function. *Nano Lett* **2020**, *20* (10), 7304–7312. https://doi.org/10.1021/acs.nanolett.0c02683.

(18) Felix Benz; Mikolaj K. Schmidt; Alexander Dreismann; Rohit Chikkaraddy; Yao Zhang; Angela Demetriadou; Cloudy Carnegie; Hamid Ohadi; Bart de Nijs; Ruben Esteban; Javier Aizpurua; Jeremy J. Baumberg. Single-Molecule Optomechanics in "Picocavities." *Science (1979)* **2016**, *354* (6313), 722–726. https://doi.org/10.1126/science.aag1322.

(19) De Angelis, F.; Gentile, F.; Mecarini, F.; Das, G.; Moretti, M.; Candeloro, P.; Coluccio, M. L.; Cojoc, G.; Accardo, A.; Liberale, C.; Zaccaria, R. P.; Perozziello, G.; Tirinato, L.; Toma, A.; Cuda, G.; Cingolani, R.; Di Fabrizio, E. Breaking the Diffusion Limit with Super-Hydrophobic Delivery of Molecules to Plasmonic Nanofocusing SERS Structures. *Nat Photonics* **2011**, *5* (11), 682–687. https://doi.org/10.1038/nphoton.2011.222.

(20) Zhang, H.; Oellers, T.; Feng, W.; Abdulazim, T.; Saw, E. N.; Ludwig, A.; Levkin, P. A.; Plumeré, N. High-Density Droplet Microarray of Individually Addressable Electrochemical Cells. *Anal Chem* **2017**, *89* (11), 5832–5839. https://doi.org/10.1021/acs.analchem.7b00008.

(21) Chen, X.; Ding, Q.; Bi, C.; Ruan, J.; Yang, S. Lossless Enrichment of Trace Analytes in Levitating Droplets for Multiphase and Multiplex Detection. *Nat Commun* **2022**, *13* (1). https://doi.org/10.1038/s41467-022-35495-9.

(22) Rana, A., Renault, C., & Dick, J. E. (2023). Measuring Liquid-into-Liquid Diffusion Coefficients by Dissolving Microdroplet Electroanalysis. *Anal. Chem. 2023, XXXX, XXX, XXX-XXX.* DOI: 10.1021/acs.analchem.3c03256.

(23) Ashutosh Rana, C. R. and J. E. D. Understanding Dynamic Voltammetry in a Dissolving Microdroplet. **2023**.

(24) Bard, A. J.; Faulkner, L. R. *Electrochemical Methods : Fundamentals and Applications*.

(25) Su, B.; Hatay, I.; Ge, P. Y.; Mendez, M.; Corminboeuf, C.; Samec, Z.; Ersoz, M.; Girault, H. H. Oxygen and Proton Reduction by Decamethylferrocene in Non-Aqueous Acidic

Media. *Chemical Communications* **2010**, *46* (17), 2918–2919. https://doi.org/10.1039/b926963k.
(26) Stauber, J. M.; Wilson, S. K.; Duffy, B. R.; Sefiane, K. On the Lifetimes of Evaporating Droplets. *J Fluid Mech* **2014**, *744*. https://doi.org/10.1017/jfm.2014.94.
(27) Wilson, S. K.; Ambrosio, H.-M. D. '. Evaporation of Sessile Droplets. *Annual Review of Fluid Mechanics Annu. Rev. Fluid Mech. 2023* **2022**, *55*, 481–509. https://doi.org/10.1146/annurev-fluid-031822.

For Table of Contents Only